JACS
JOURNAL OF THE AMERICAN CHEMICAL SOCIETY

ARTICLE

pubs.acs.org/JACS

Predicted Electronic and Thermodynamic Properties of a Newly Discovered Zn_8Sb_7 Phase

Gregory S. Pomrehn,* Eric S. Toberer,† G. Jeffrey Snyder, and Axel van de Walle

Materials Science, California Institute of Technology, 1200 East California Boulevard, Pasadena, California 91125, United States

ABSTRACT: A new binary compound, Zn_8Sb_7, has recently been prepared in nanoparticulate form via solution synthesis. No such phase is known in the bulk phase diagram; instead, one would expect phase separation to the good thermoelectric semiconductors ZnSb and Zn_4Sb_3. Here, density functional calculations are employed to determine the free energies of formation, including effects from vibrations and configurational disorder, of the relevant phases, yielding insight into the phase stability of Zn_8Sb_7. Band structure calculations predict Zn_8Sb_7, much like ZnSb and Zn_4Sb_3, to be an intermetallic semiconductor with similar thermoelectric properties. If sufficient entropy or surface energy exists to stabilize the bulk material, it would be stable in a limited temperature window at high temperature.

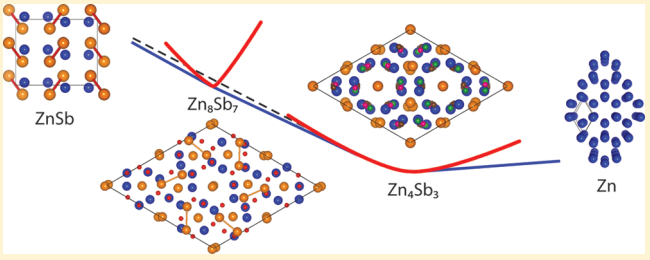

INTRODUCTION

Intermetallic compounds are fascinating due to the diversity of their crystal structures and resulting properties. For thermoelectric applications, ZnSb and Zn_4Sb_3 are two intermetallic compounds which exhibit good thermoelectric efficiencies. In particular, Zn_4Sb_3 has a thermoelectric figure of merit (zT) in excess of unity[1,2] due to its low thermal conductivity, which arises in part due to its complex, defect-ridden structure. Both of these materials have band gaps at or near the Fermi level which can be rationalized from valence charge counting.[3]

Recently, a new binary Zn−Sb phase between ZnSb and Zn_4Sb_3 was discovered and characterized at room temperature by Birkel et al.[4] Binary nanoparticles were synthesized in solution through the controlled reaction of elemental Zn and Sb nanoparticles. The small particle size of the reactants ensures minimum diffusion paths, low activation barriers, and low reaction temperatures, thereby eliminating solid−solid diffusion as the rate-limiting step as found in conventional bulk-scale solid-state synthesis.[4] In the present work, the authors denote this new phase as Zn_8Sb_7, based on the idealized crystal structure, rather than $Zn_{1+\delta}Sb$ (with $\delta = 0.068$) as used in ref 4.

Determination of the Zn_8Sb_7 structure was a *tour de force* of automated electron diffraction tomography (ADT) combined with precession electron diffraction (PED) on individual nanoparticle grains. This work yielded the structure in Figure 1, shown along the [001] and [100] directions in the distorted hexagonal cell ($P\bar{1}$). Much like Zn_4Sb_3, Zn_8Sb_7 contains both Sb_2^{4-} dimers and isolated Sb^{3-}; however, the long-range atomic arrangement is completely distinct.

The Zn_8Sb_7 phase enters into an interesting region of the binary phase diagram[5] between ZnSb and Zn_4Sb_3. Since the three phases are so close in composition, the competition for thermodynamic stability will be fierce. Below ~250 K, Zn_4Sb_3 transforms to a variant (the α or α′ phase) where the interstitial atoms form an ordered arrangement.[6,7] The disordered β phase is stable from ~250 K (to 700 K), while no compounds have been characterized in the bulk at compositions between Zn_4Sb_3 and ZnSb. Several phase diagrams have been reported that include a phase between Zn_4Sb_3 and ZnSb stable only at high temperature,[5,8,9] sometimes denoted as γ, but no crystal structures have been determined for these high-temperature phases.

Ab initio calculations have considered various interstitial configurations of Zn_4Sb_3 at 0 K and found that they should decompose to ZnSb and Zn when considering the enthalpy of formation alone.[10−13] Additional theoretical work has recently shown Zn_4Sb_3 to be entropically stabilized due to the high configurational disorder with the three interstitial Zn sites and the effects of lattice vibrations.[14] The narrow stable composition range is near $Zn_{3.898}Sb_3$, as inferred from hall carrier measurements and valence charge counting,[2,14] which is off from the valence-balanced composition of $Zn_{3.9}Sb_3$. We will continue to use the conventional Zn_4Sb_3 terminology.

In this work, we explore the electronic and thermodynamic properties of a theoretical bulk Zn_8Sb_7 phase. Electronic structure calculations probe the band structure and valence band edge character of Zn_8Sb_7 to compare with known bulk thermoelectrics ZnSb and Zn_4Sb_3. Since the formation of Zn_8Sb_7 is not readily observed in practice, a thermodynamic investigation determines if the phase might be thermodynamically stable or metastable with respect to competing Zn−Sb phases. A thorough thermodynamic treatment considers the bonding enthalpy as well as possible sources of entropy such as configurational disorder and

Received: March 18, 2011
Published: June 16, 2011

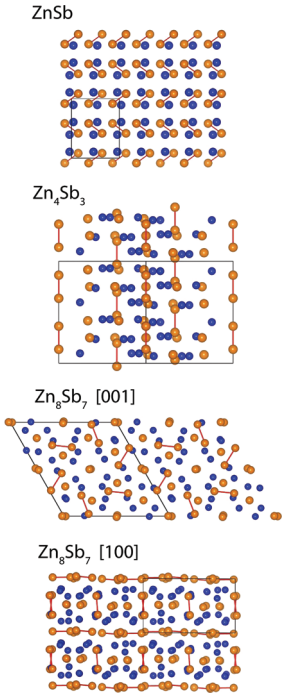

Figure 1. Structures of the known room-temperature zinc antimonide phases, shown with zinc in blue, Sb_2^{4-} dimers and isolated Sb^{3-} in orange. The anionic structure of ZnSb is exclusively Sb_2^{4-} dimers, while Zn_4Sb_3 and Zn_8Sb_7 contain both Sb^{3-} and Sb_2^{4-} moieties.

atomic vibrations. The results will guide future experiments to synthesize bulk Zn_8Sb_7.

COMPUTATIONAL METHODS

To account for the configurational disorder present in many Zn−Sb phases, a thermodynamic ensemble approach is employed using data from first-principles calculations. A Grand Canonical Potential[15] (GCP) is formulated for each phase according to

$$\phi(T,\boldsymbol{\mu}) = -\frac{k_B T}{N} ln(\sum_s e^{-(E_s - \boldsymbol{\mu}\cdot\mathbf{N}_s)/k_B T}) \quad (1)$$

where k_B is Boltzmann's constant, T is temperature, N is the total number of atoms in the system, while, for a given state s, E_s is the total energy of state, $\mathbf{N}_s$ is a vector containing the number of atoms for each chemical species (with elements summing to N), and $\boldsymbol{\mu}$ is a vector containing the chemical potential of each species. Since ZnSb and Zn phases exhibit relatively low configurational disorder, the GCP greatly simplifies:

$$\phi(T,\boldsymbol{\mu}) = \frac{\varepsilon_0}{n} - \boldsymbol{\mu}\cdot\mathbf{x_0} \quad (2)$$

where ε_0 is the energy per unit cell, n is the number of atoms per unit cell, and $\mathbf{x_0}$ is a vector of the atomic fraction of each species.

For Zn_8Sb_7 and Zn_4Sb_3, we factor the GCP according to an "independent cells" approximation. We assume that each primitive unit cell is non-interacting with neighboring cells, in the sense that the defect configuration present in one cell does not affect the energies of defect configurations in a nearby cell. (All our *ab initio* calculations are nevertheless performed on infinite periodic systems with suitable k-point sampling.) This approach is useful in these systems because the unit cells are rather large. This assumption is validated by computing the energy of supercells with different configurations in each primitive unit cell and comparing it to that predicted by summing the energies of the constituent primitive cells. Under the independent cells approximation,

$$\phi(T,\boldsymbol{\mu}) = \frac{\varepsilon_0}{n} - \boldsymbol{\mu}\cdot\mathbf{x_0} - \frac{k_B T}{n} ln(1 + \sum_{i>0} m_i\, e^{-(\Delta\varepsilon_i - \boldsymbol{\mu}\cdot\Delta\mathbf{n}_i)/k_B T}) \quad (3)$$

where ε_0 is the ground-state energy per unit cell, n is the number of atoms per unit cell, and $\mathbf{x_0}$ is the ground-state composition. For each configuration i, m_i is the symmetric multiplicity, $\Delta\varepsilon_i$ is the change in energy from the ground state, and $\Delta\mathbf{n}_i$ is the change in the number of atoms from the ground state.

The total energy of each atomic configuration was calculated using Density Functional Theory (DFT) with the PBE exchange-correlation functional.[16] Calculations utilized the projector augmented wave (PAW) method[17] as implemented in VASP,[18] neglecting spin−orbit coupling. All unit cell parameters and atomic positions were allowed to relax to find the lowest energy arrangement to within 10^{-4} eV per primitive unit cell. A final static calculation was performed for an accurate total energy. Energy convergence with respect to k-points was achieved with a Γ-centered grid with 14 k-points in the irreducible Brillouin zone.

Configurational arrangements for Zn_4Sb_3 were enumerated by considering all possible interstitial combinations on known Zn interstitial sites.[3,14] Configurational arrangements of Zn_8Sb_7 are much more difficult to enumerate appropriately without guidance from experimentally known defect lattice sites. The configurational disorder then was probed by a systematic enumeration of new possible configurations on the Zn sublattice. The specific enumeration process is described later in the Results and Discussion. Configurations with Zn vacancies and interstitials deviating from the Zn_8Sb_7 composition are also considered. DFT calculations were performed on select Zn_8Sb_7 configurations since it would be computationally prohibitive to calculate all possibilities. Atomic positions were allowed to relax to a local minimum and were verified to not have settled into identical configurations. While this method is by no means exhaustive in gauging the configurational disorder in Zn_8Sb_7, it does provide a basis for making certain assumptions, to follow in the Results and Discussion.

Phonon density of states and vibrational free energies were calculated using the "supercell" method as implemented in the Alloy Theoretic Automated Toolkit (ATAT).[19−21] The computational resources needed to compute phonon modes for all Zn_8Sb_7 configurations are prohibitive (360 perturbation structures per configuration per volume), so the phonon modes were only calculated for the nominal configuration. In all, phonon modes were calculated for one Zn_8Sb_7 configuration and several Zn_4Sb_3 configurations as well as end-members Zn and ZnSb at 0%, 1%, and 2% strain to account for the effects of thermal expansion under the quasi-harmonic approximation.

The vibrational contribution to the free energy is incorporated into the GCP through a nested sum in the partition function.[22] For each distinct configuration, phonon occupation accounts for small displacements around the local energy minimum, resulting in a temperature-dependent free energy correction.

GCPs were assembled for Zn, Zn_4Sb_3, Zn_8Sb_7, and ZnSb. Phase equilibrium is determined by equality of two respective GCPs. The equilibrium composition of each phase can be determined by

$$\nabla_{\boldsymbol{\mu}}\phi(T,\boldsymbol{\mu}) = -\mathbf{x} \quad (4)$$

and the free energy is calculated as

$$f(T,\mathbf{x}) = \phi(T,\boldsymbol{\mu}_\mathbf{x}) + \boldsymbol{\mu}_\mathbf{x}\cdot\mathbf{x} \quad (5)$$

where $\mu_\mathbf{x}$ is the chemical potential that stabilizes the phase at composition $\mathbf{x}$.

The Seebeck coefficient is calculated for the ground-state structures using the Boltzmann transport equation within the constant relaxation

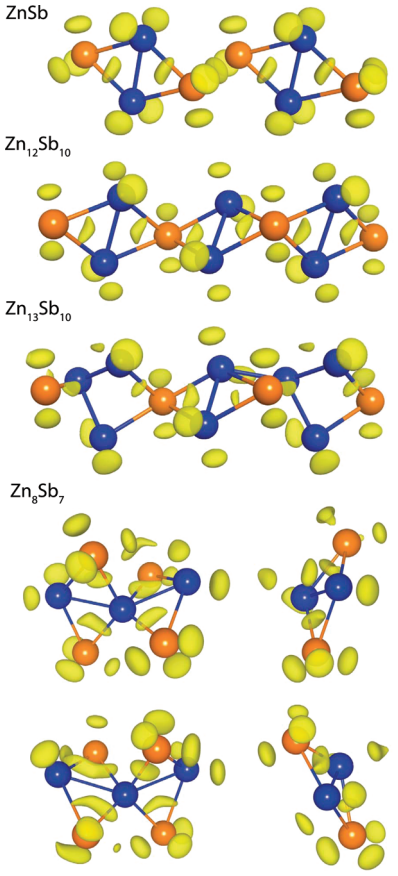

Figure 2. Electron density difference plots showing networked structures of diamond moieties of ZnSb, Zn_4Sb_3, and Zn_8Sb_7. Yellow isosurfaces show regions of electron accumulation with respect to unperturbed overlapping atomic wave functions. In all structures, Sb atoms share a local maximum "banana" with two closely spaced Zn atoms, forming diamond-shaped moieties. The network of diamonds becomes increasingly complex in Zn_4Sb_3 and Zn_8Sb_7, providing a rich source of entropy.

time approximation as implemented in the BoltzTraP code.[23] A dense *k*-point mesh is required to evaluate the Fermi integrals over the entire Brillouin zone. Convergence of the Seebeck coefficient with respect to carrier concentration is achieved in Zn_8Sb_7 with a 14×14×14 Γ-centered *k*-point grid. For Zn_4Sb_3 and ZnSb structures, 16×16×16 and 40×32×32 *k*-point grids are used, respectively.

RESULTS AND DISCUSSION

Crystal Structure and Charge Counting. The Zn−Sb structures in Figure 1 can all be described using the Zintl−Klemm formalism,[24] in which Zn cations donate electrons to Sb anions which may then form covalent bonds with other Sb to complete their valence shells. A molecular orbital (MO) approach, which includes interactions between Zn and Sb, can also successfully rationalize the electron count.[13] In ZnSb (*Pbca*), all the respective Zn and Sb atoms are symmetrically equivalent. The Zn cations each donate two electrons to an Sb anion, and the Sb atoms form Sb_2^{4-} dimers. A valence-precise structure results with 8 Zn^{2+} and 4 Sb_2^{4-} per unit cell. One then can rationalize why ZnSb behaves electronically as an intrinsic semiconductor with a band gap between the valence band (dominated by Sb

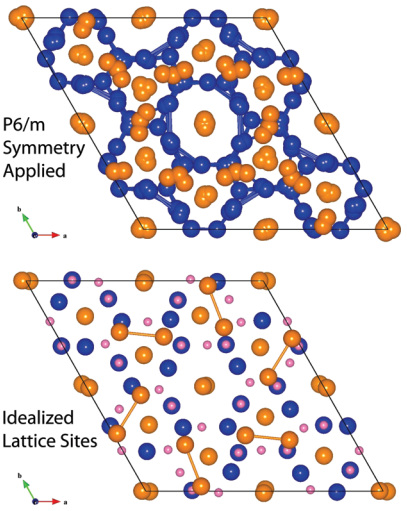

Figure 3. (Top) Zn_8Sb_7 lattice sites after applying all 12 symmetry operations of the *P6/m* space group. The orange Sb sites map relatively closely to the original sites. Many of the blue Zn sites map to new sites, while a few map to nearly symmetrically equivalent sites. (Bottom) Idealized lattice sites after removing nearly equivalent sites. The original 28 Sb sites and 32 Zn sites are in orange and blue, respectively. An additional 66 unique Zn interstitial sites are shown in pink.

p-states) and the conduction band (composed primarily of Zn s-states).

The Zn_4Sb_3 ($R\bar{3}c$) framework structure is composed of 30 Sb (orange sites in Figure 1) and 36 Zn (blue sites) in the conventional unit cell. The anionic framework is divided between 6 Sb_2^{4-} dimers and 18 isolated Sb^{3-}. A fully occupied cation framework of 36 Zn^{2+} is insufficient to satisfy a valence charge balance. Three additional Zn^{2+} are needed to satisfy the charge balance at a composition of $Zn_{13}Sb_{10}$. These additional Zn atoms can occupy any of three symmetrically distinct regions for interstitial sites (pink, green, and brown sites), introducing configurational disorder not present in ZnSb. Thermodynamically, Zn_4Sb_3 is stable only in a narrow range of composition near $Zn_{12.992}Sb_{10}$, which is slightly valence deficient. This explains the persistent p-type doping observed experimentally in Zn_4Sb_3.

Examining the Zn_8Sb_7 ($P\bar{1}$) structure reveals some similarities to Zn_4Sb_3. The anionic Sb framework is only slightly distorted from a high-symmetry structure that can be described with a *P6/m* space group. There are 10 Sb_2^{4-} dimers and 8 isolated Sb^{3-}, all sitting close to points of symmetry. The cation Zn framework exhibits low symmetry with 32 Zn^{2+}. This satisfies a valence-precise condition, suggesting that Zn_8Sb_7, like ZnSb and $Zn_{13}Sb_{10}$, should behave as an intrinsic semiconductor.

We further investigate the structure of Zn_8Sb_7 with the help of electron density difference (EDD) plots. The EDD compares the calculated electron charge density with the charge density resulting from the overlap of non-interacting single-atom electronic wave functions. EDD plots thus reveal where charge accumulation and depletion occur as atomic wave functions interact. Charge accumulation between atoms suggests the presence of a covalent bond.

Figure 2 shows the EDD around a diamond moiety in ZnSb, which clearly reveals charge accumulation lobes in a tetrahedral arrangement around each Sb atom. In agreement with a previous molecular orbital study,[13] one lobe of each Sb is shared between two closely spaced Zn atoms, forming a repeated diamond unit.

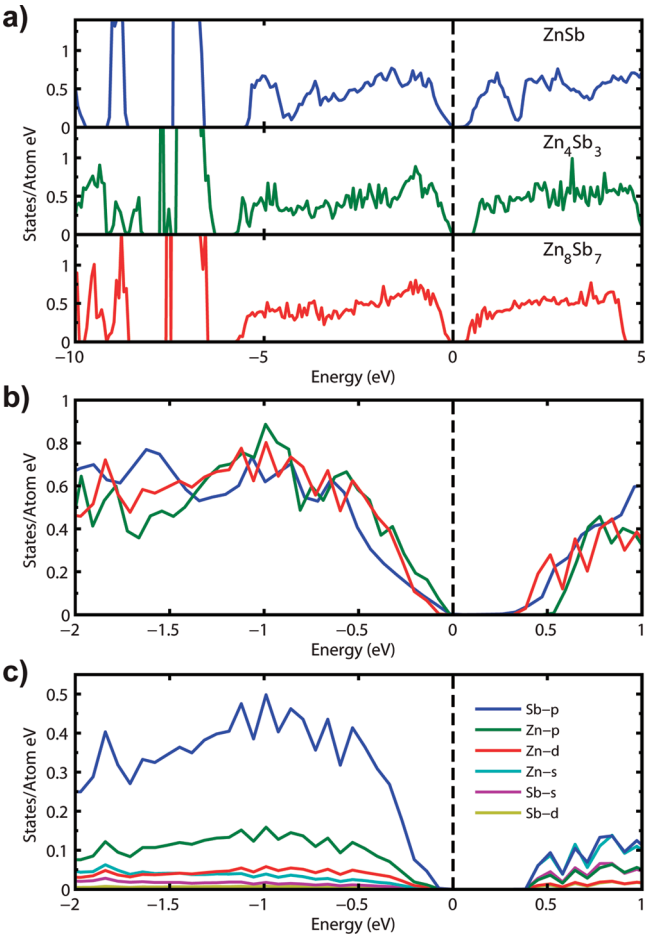

Figure 4. (a) Calculated density of states for of ZnSb, Zn_4Sb_3, and Zn_8Sb_7. (b) Comparison near the Fermi level and (c) atomic orbital projected density of states for Zn_8Sb_7.

This same diamond moiety is also apparent in Zn_4Sb_3. Figure 2 shows the EDD for a configuration of composition $Zn_{12}Sb_{10}$ (no interstitial Zn). In this case, each lone Sb atom shares a lobe with each of two pairs of Zn atoms, forming zigzag chains of diamond moieties.[13] The Sb dimers form a separate linear chain from the diamonds. The presence of interstitial Zn, such as in $Zn_{13}Sb_{10}$ configurations, breaks up the chain and creates local disorder in the diamond network. High configurational entropy results because there are many possible ways for the interstitial Zn to distort and rearrange the diamond network, all with similar energetic consequences.

In Zn_8Sb_7, we again see the diamond moiety but with added complexity. Nonlinear chains of diamond moieties incorporate both Sb dimers (as in ZnSb) and lone Sb (as in Zn_4Sb_3). All the diamonds are distorted out of plane, as is shown for two of the diamonds in Figure 2. The crystal structure is frustrated in the sense that it cannot settle into a single preferred ordered state, such as in ZnSb, but like Zn_4Sb_3, there are many configurational possibilities that result in similar energetics.

One way to enumerate the possible configurational states is to consider the mismatch of symmetry between the Sb and Zn sublattices. There are six symmetrically equivalent ways to combine the higher symmetry $P6/m$ Sb sublattice with the lower symmetry $P\bar{1}$ Zn sublattice. By combining these six arrangements into a single lattice, one can discover possible interstitial sites on the Zn sublattice. The combined lattice is shown in Figure 3. All the orange Sb sites map closely to existing sites, as expected. However, the blue Zn sites reveal many new locations. Nearly equivalent sites are combined to form an idealized lattice with 66 new possible Zn sites, shown in pink at the bottom of Figure 3. These sites provide a basis to probe the configurational disorder. Configurational arrangements involving Zn vacancies on the highly occupied blue sites and Zn interstitials on partially occupied pink sites can be enumerated and the energies calculated from first-principles calculations. This configurational disorder could likely be undetected by electron diffraction analysis due to the low occupation of certain sites. The experimentally predicted[4] partial occupancy results in a composition of $Zn_{29.9}Sb_{28}$, which could be explained as an average of 2.1 Zn atoms per unit cell occupying various interstitial sites. The entropy associated with this disorder will be addressed in the Phase Stability section.

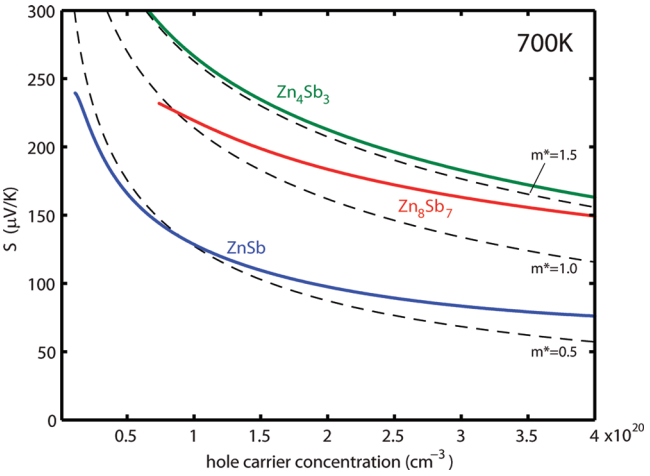

Figure 5. Calculated Seebeck coefficient as a function of (hole) carrier concentration assuming a rigid band model for ZnSb, Zn_4Sb_3, and Zn_8Sb_7. Dashed lines correspond to calculations from a single parabolic band model with effective carrier mass m^* under the constant relaxation time approximation.

Electronic Structure. The calculated electronic density of states of Zn_8Sb_7 is shown in Figure 4, along with those for ZnSb and Zn_4Sb_3. As expected from the Zintl–Klemm charge counting, Zn_8Sb_7 is found to be an intrinsic semiconductor like ZnSb and Zn_4Sb_3. The calculated band gap is comparable to that of ZnSb but slightly smaller than that of Zn_4Sb_3. The similar shape and magnitude of the valence band edges of Zn_8Sb_7 and Zn_4Sb_3 suggest a similar hole carrier effective mass. This result alone suggests that Zn_8Sb_7 might have electronic properties similar to those of Zn_4Sb_3. The valence band edge is composed primarily of electronic states localized around the nonbonded Sb atoms. The projected density of states in Figure 4 shows that the valence band is composed primarily of Sb p-orbital character, which is similar to previous studies of Zn_4Sb_3 and ZnSb.[13]

The calculated Seebeck coefficient, S, as a function of (hole) carrier concentration is shown in Figure 5 for 700 K. This assumes a rigid band model with a carrier concentration controlled by shifting the electronic chemical potential away from the intrinsic Fermi energy. For reference, dashed lines show trends derived from a single parabolic band approximation for an effective carrier mass, m^*. The Seebeck coefficient of Zn_8Sb_7 approaches that of Zn_4Sb_3 at higher carrier concentrations for similar doping levels. An optimum carrier concentration can be

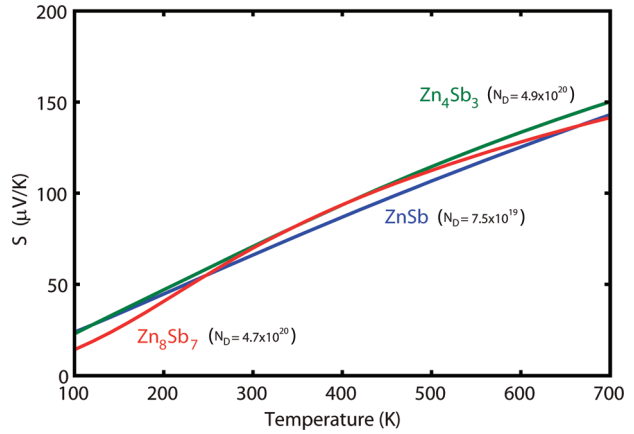

Figure 6. Calculated Seebeck coefficient as a function of temperature at constant carrier concentration (assuming extrinsic doping regime). Carrier concentration is chosen to maximize the power factors of the respective phases under the constant relaxation time approximation.

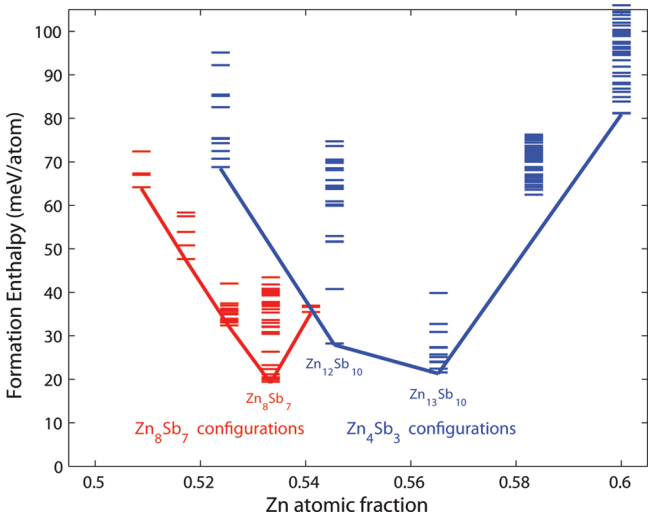

Figure 7. Formation enthalpy with respect to Zn and ZnSb at 0 K for Zn_8Sb_7 (red) and Zn_4Sb_3 (blue) configurations. The lines connect the respective lowest energy configurations at each composition.

chosen to maximize the power factor, σS^2, with electrical conductivity, σ, calculated under the constant relaxation time approximation. An approximate relaxation time is found by fitting to experimental resistivity data for ZnSb[25] and Zn_4Sb_3[2] and assuming a similar value for Zn_8Sb_7. The constant carrier concentration Seebeck coefficient as a function of temperature is shown in Figure 6. Both Zn_4Sb_3 and Zn_8Sb_7 have a maximum power factor for a hole concentration of around 5×10^{20} cm^{-3} and ZnSb for a concentration of 7.5×10^{19} cm^{-3}. It should be noted that in ZnSb it has proven difficult to achieve hole concentrations above 10^{19} cm^{-3}. In Zn_4Sb_3 single-phase material, the hall carrier concentration ranges between 6×10^{19} and 9×10^{19} cm^{-3}.

Phase Stability. Finally, we consider the thermodynamic phase stability of this new Zn_8Sb_7 phase. We note that for Zn_8Sb_7 to be thermodynamically stable, the free energy must fall below the tie-line between ZnSb and Zn_4Sb_3. This will prove difficult for Zn_8Sb_7, as Zn_4Sb_3 has high entropy even at room temperature. We start by considering the formation enthalpy at 0 K and then include entropic contributions at finite temperature.

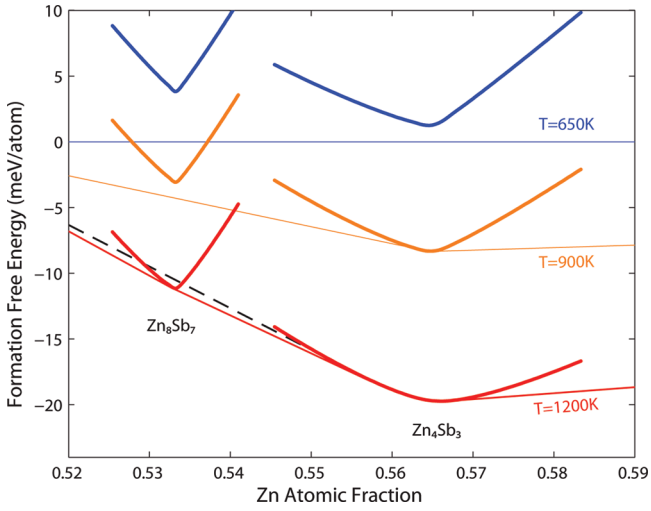

Figure 8. Calculated formation free energy curves for Zn_4Sb_3 and Zn_8Sb_7 with respect to ZnSb and Zn at three temperatures. A convex hull is drawn connecting the free energy curves of the thermodynamically stable phase at a given temperature. At 650 K, Zn and ZnSb are in equilibrium over the entire composition range shown. At 900 K, Zn_4Sb_3 has broken the convex hull and has a pure phase stability window on a narrow composition range. At 1200 K, Zn_8Sb_7 has broken the convex hull and shows a favorable formation energy with respect to ZnSb and Zn_4Sb_3 (connected by the black dashed line).

Figure 7 shows the calculated formation enthalpy of Zn_8Sb_7 configurations (red) alongside those of Zn_4Sb_3 (blue). We readily observe that Zn_8Sb_7 configurations have positive formation enthalpy with respect to decomposition into ZnSb and Zn. This is perhaps not unexpected due to similarities with Zn_4Sb_3, which also has positive formation enthalpy at 0 K. However, Zn_4Sb_3 is known to be thermodynamically stable at higher temperatures[14] due to both configurational and vibrational entropic contributions to the free energy. These sources might have significant contributions for Zn_8Sb_7 as well.

Entropy arises in an ensemble when many configurations are energetically accessible. It is apparent from Figure 7 that we will expect some configurational entropy in Zn_8Sb_7 at finite temperature from the several configurations with similar formation energy. Due to computational limitations on the large unit cell, we have only calculated 30 different configurations at the $Zn_{32}Sb_{28}$ composition as well as 30 off-stoichiometric configurations. These known configurations represent only a small subset of the possible arrangements of atoms that can be enumerated on the basis of the idealized lattice in Figure 3. Each of our known configurations is likely representative of many other configurations of similar energy. To estimate this, we consider the "mean field" entropy based on the average fractional occupancy, x_i of each site, i:

$$S_{mf}[k_B/cell] = -k_B \sum_i [x_i \ln(x_i) + (1 - x_i)\ln(1 - x_i)] \quad (6)$$

We can correct this value by assuming that Zn_8Sb_7 deviates from the mean field value similarly to Zn_4Sb_3. For Zn_4Sb_3, considering 90% occupancy on the framework sites and 5% occupancy on each of three interstitial sites gives an average mean field entropy of 0.48 k_B/atom. This is almost twice as high as the configurational entropy calculated from the grand canonical ensemble, 0.21 k_B/atom. For Zn_8Sb_7, we consider a Zn

Table 1. Bulk Moduli, B, as Fit to the Equation of State, $E(V) = (B/2V_0)(V - V_0)^2$ (for Total Energy, E, Unit Cell Volume, V, and Ground-State Volume, V_0), and the Room Temperature Unit Cell Volume (Calculated and Measured) for Three Zn−Sb Phases

	bulk modulus		unit cell volume (Å^3)		
	eV/Å^3	GPa	DFT (GGA)	exptl	error (%)
Zn_4Sb_3	0.267	42.7	571	536	2.1
Zn_8Sb_7	0.240	38.5	1577	1625	−1.0
ZnSb	0.248	39.7	410	391	1.6

framework site occupancy of 93% based on the experimentally determined partial occupancy. The remaining Zn is interspersed over 66 possible interstitial sites. This results in a mean field entropy of 0.28 k_B/atom, which we reduce by the correction factor for Zn_4Sb_3 to estimate the configurational entropy for Zn_8Sb_7 as 0.12 k_B/atom. The GCP (eq 3) for Zn_8Sb_7 is tuned by increasing the multiplicative constants, m_i, so that, in the high-temperature limit, $S = -\partial\varphi/\partial T = 0.12\ k_B$/atom (the adjusted mean field entropy). In essence, this procedure combines enthalpy obtained from the *ab initio* calculations with an entropy estimate based on structural similarities with the Zn_4Sb_3 phase.

The vibrational contributions to the free energy have also been accounted for in the quasiharmonic approximation. Both Zn_4Sb_3 and Zn_8Sb_7 have a favorable contribution to the free energy from phonons with respect to Zn and ZnSb. In the high-temperature limit above 300 K, Zn_8Sb_7 has an approximate vibrational entropy of 0.19 k_B/atom, which is slightly less than that of Zn_4Sb_3, 0.22 k_B/atom.

The GCP for each phase was calculated according to eq 3, and the boundary lines of phase equilibria were determined by equality of two respective GCPs. Formation free energy curves, as a function of composition, are shown for Zn_8Sb_7 and Zn_4Sb_3 at three different temperatures in Figure 8. The set of blue curves at 650 K correspond to the region of phase decomposition into ZnSb and Zn. At the intermediate temperature in orange, the formation free energy of Zn_4Sb_3 has dropped below those of Zn and ZnSb. The convex hull connects the lowest energy phase at each composition and includes the respective common tangent construction between Zn_4Sb_3, ZnSb, and Zn. At this temperature, there is no thermodynamic stability for Zn_8Sb_7, even though it is more favorable than decomposition to ZnSb and Zn. At the highest temperature in red, we see that the Zn_8Sb_7 free energy curve touches the convex hull, indicating a region of phase stability. The black dashed line indicates the convex hull without the Zn_8Sb_7 phase. We see that Zn_8Sb_7 could have a temperature window of phase stability at high temperature, if there is sufficient entropy as in our estimation. We note that the calculated temperature scale does not correspond exactly to the physical Kelvin scale. Our temperatures likely overpredict the stabilization temperatures for both Zn_4Sb_3 and Zn_8Sb_7.

With our plausible assumptions for configurational entropy, we show that Zn_8Sb_7 can be thermodynamically stable at high temperatures. We also consider two possible reasons as to why Zn_8Sb_7 has only been observed experimentally in nanoparticulate form: lattice strain and surface energy. *Ab initio* calculations under the GGA typically overestimate the experimentally observed lattice parameter. This is indeed the case with ZnSb and Zn_4Sb_3, for which calculations predict, respectively, a 1.6% and 2.1% lattice parameter overestimation at 300 K (including the calculated thermal expansion due to lattice vibrations). We would expect to see a linear trend with composition between ZnSb and Zn_4Sb_3.[26] Contrary to expectation, the calculated lattice parameter of Zn_8Sb_7 underpredicts the experimentally characterized lattice parameter by 1.0% at 300 K, as shown in Table 1. This error is likely within the limits of accuracy for the experimentally characterized lattice constant, but the presence of lattice strain is possible, due to either a surface stress or other synthetic factors.

Surface effects could explain the more favorable formation of Zn_8Sb_7 in nanoparticulate form. If the surface energy of Zn_8Sb_7 was lower than the average surface energy of ZnSb and Zn_4Sb_3, then for a fixed number of atoms in a nanoparticle, we would expect Zn_8Sb_7 to be more favored for small particle sizes. Calculating the surface energy for each of these structures would be computationally prohibitive, but we can consider values that might be plausible. As an example, if Zn_8Sb_7 has a lower surface energy than ZnSb and Zn_4Sb_3 by 0.05 eV/Å^2 (0.78 J/m^2, which is on the order of differences reported in some elemental surface energies[27]), then for a 50 nm particle, Zn_8Sb_7 would have an energy benefit of 6 meV/atom with respect to ZnSb and Zn_4Sb_3. At a particle size of 90 nm, the surface energy difference would be negligible. Even if we assume that the surface energy is constant between all phases, we still observe that Zn_8Sb_7 has a lower bulk modulus than both ZnSb and Zn_4Sb_3 (Table 1). In a stressed surface condition, we expect the softer phase, Zn_8Sb_7, to have a more significant energy lowering to the surface contribution according to $P^2/2B$, where P is pressure and B is the bulk modulus. Thus, Zn_8Sb_7 would be slightly favored over ZnSb and Zn_4Sb_3. At the pressure required to adjust the calculated Zn_8Sb_7 lattice parameter to the experimental value (−3.4 GPa), the energy correction is 3 meV/atom in favor of Zn_8Sb_7. We suggest that through some combination of surface energy and lattice strain, Zn_8Sb_7 might be more favorable under certain conditions.

CONCLUSIONS

From our first-principles investigation of Zn_8Sb_7, we expect the theoretical bulk Zn_8Sb_7 phase to exhibit good thermoelectric properties. We predict Zn_8Sb_7 to be entropically stabilized at high temperature if our assumption of configurational entropy holds true. There are also other mechanisms, such as lattice strain or surface energy, that would favor the stability of Zn_8Sb_7 with respect to ZnSb and Zn_4Sb_3. The stability of Zn_8Sb_7 at high temperatures could partially explain the complexity observed in this part of the Zn−Sb phase diagram.

AUTHOR INFORMATION

Corresponding Author
gpomrehn@caltech.edu

Current Address
[†]Physics Department, Colorado School of Mines, Golden, Colorado 80401, United States.

ACKNOWLEDGMENT

This work is supported by the U.S. National Science Foundation via Grant No. DMR-0953378, through TeraGrid resources at NCSA and SDSC under Grant No. TGDMR050013N, the ARO-MURI Materials on the Brink, and the DARPA Nano Materials Program.

REFERENCES

(1) Caillat, T.; Fleurial, J.-P.; Borshchevsky, A. *J. Phys. Chem. Solids* **1997**, *58*, 1119–1125.
(2) Toberer, E. S.; Rauwel, P.; Gariel, S.; Tafto, J.; Jeffrey Snyder, G. *J. Mater. Chem.* **2010**, *20*, 9877–9885.
(3) Snyder, G.; Christensen, M.; Nishibori, E.; Caillat, T.; Iversen, B. *Nat. Mater.* **2004**, *3*, 458–463.
(4) Birkel, C. S.; Mugnaioli, E.; Gorelik, T.; Kolb, U.; Panthöfer, M.; Tremel, W. *J. Am. Chem. Soc.* **2010**, *132*, 9881–9889.
(5) Izard, V.; Record, M.; Tedenac, J. *J. Alloys Compd.* **2002**, *345*, 257–264.
(6) Nylen, J.; Andersson, M.; Lidin, S.; Haussermann, U. *J. Am. Chem. Soc.* **2004**, *126*, 16306–16307.
(7) Nylen, J.; Lidin, S.; Andersson, M.; Iversen, B. B.; Newman, N.; Haussermann, U. *Chem. Mater.* **2007**, *19*, 834–838.
(8) Li, J.-B.; Record, M.-C.; Tedenac, J.-C. *J. Alloys Compd.* **2007**, *438*, 171–177.
(9) Liu, X.; Wang, C.; Ohnuma, I.; Kainuma, R.; Ishida, K. *J. Phase Equilib.* **2000**, *21*, 432–442.
(10) Kim, S.-G.; Mazin, I. I.; Singh, D. J. *Phys. Rev. B* **1998**, *57*, 6199–6203.
(11) Cargnoni, F.; Nishibori, E.; Rabiller, P.; Bertini, L.; Snyder, G. J.; Christensen, M.; Gatti, C.; Iversen, B. B. *Chem.—Eur. J.* **2004**, *10*, 3861–3870.
(12) Toberer, E. S.; Sasaki, K. A.; Chisholm, C. R. I.; Haile, S. M.; Goddard, W. A., III; Snyder, G. J. *Phys. Stat. Sol. RRL* **2007**, *1*, 253–255.
(13) Mikhaylushkin, A. S.; Nylen, J.; Haussermann, U. *Chem.—Eur. J.* **2005**, *11*, 4912–4920.
(14) Pomrehn, G. S.; Toberer, E. S.; Snyder, G. J.; van de Walle, A. *Phys. Rev. B* **2011**, *83*, 094106.
(15) van de Walle, A.; Asta, M. *Modelling Simul. Mater. Sci. Eng.* **2002**, *10*, 521.
(16) Perdew, J. P.; Burke, K.; Ernzerhof, M. *Phys. Rev. Lett.* **1996**, *77*, 3865.
(17) Blöchl, P. E. *Phys. Rev. B* **1994**, *50*, 17953.
(18) Kresse, G.; Furthmüller, J. *Comput. Mater. Sci.* **1996**, *6*, 15.
(19) van de Walle, A.; Asta, M.; Ceder, G. *CALPHAD J.* **2002**, *26*, 539.
(20) van de Walle, A. *CALPHAD J.* **2009**, *33*, 266.
(21) van de Walle, A.; Ceder, G. *J. Phase Equilib.* **2002**, *23*, 348.
(22) van de Walle, A.; Ceder, G. *Rev. Mod. Phys.* **2002**, *74*, 11.
(23) Madsen, G.; Singh, D. *Comput. Phys. Commun.* 2006, 175.
(24) Kauzlarich, S. M. *Chemistry, Structure, and Bonding of Zintl Phases and Ions*; Wiley-VCH: Weinheim1996.
(25) Bottger, P. H. M.; Pomrehn, G. S.; Snyder, G. J.; Finstad, T. G., submitted.
(26) van de Walle, A.; Ceder, G. *Phys. Rev. B* **1999**, *59*, 14992.
(27) Skriver, H. L.; Rosengaard, N. M. *Phys. Rev. B* **1992**, *46*, 7157–7168.